A Highly Porous Copper Electrocatalyst for Carbon Dioxide Reduction

Jing-Jing Lv, Matthew Jouny, Wesley Luc, Wenlei Zhu, Jun-Jie Zhu, and Feng Jiao*

Electrochemical reduction of carbon dioxide (CO_2) is an appealing approach toward tackling climate change associated with atmospheric CO_2 emissions. This approach uses CO_2 as the carbon feedstock to produce value-added chemicals, resulting in a carbon-neutral (or even carbon-negative) process for chemical production. Many efforts have been devoted to the development of CO_2 electrolysis devices that can be operated at industrially relevant rates; however, limited progress has been made, especially for valuable C_{2+} products. Herein, a nanoporous copper CO_2 reduction catalyst is synthesized and integrated into a microfluidic CO_2 flow cell electrolyzer. The CO_2 electrolyzer exhibits a current density of 653 mA cm^{-2} with a C_{2+} product selectivity of ≈62% at an applied potential of –0.67 V (vs reversible hydrogen electrode). The highly porous electrode structure facilitates rapid gas transport across the electrode–electrolyte interface at high current densities. Further investigations on electrolyte effects reveal that the surface pH value is substantially different from the pH of bulk electrolyte, especially for nonbuffering near-neutral electrolytes when operating at high currents.

Current commodity chemicals are largely based on fossil fuel–derived carbon sources such as coal and crude oil. Using carbon dioxide (CO_2) as an alternative carbon feedstock is an attractive approach toward tackling CO_2 emissions in the chemical industry because it can drastically reduce or even result in negative carbon footprint,[1–4] whereas traditional chemical processes such as steam methane reforming and coal gasification are carbon intensive. CO_2 reduction can be performed through biological, thermochemical, photochemical, and electrochemical means, each of which has been widely studied.[3,5,6] Among all potential approaches, electrochemical conversion of CO_2 has attracted much attention because this technology has several advantages over other competitive technologies, including

fine control of production rates, wide scalability of modular electrolyzer designs, and the potential to produce a variety of high-value products.[7–9] More importantly, this technology can be readily powered by carbon-free energy sources such as wind, solar, and nuclear, providing a zero-CO_2 emission (or even negative) pathway for commodity chemical production. A recent scientific study on photovoltaic (PV) clearly showed a decrease of PV electricity price over time with a projected PV electricity price as low as $0.03 per kWh in the near future.[10] A similar trend also holds for wind energy with an electricity price already being ≈$0.02 per kWh.[11] Thus, the low electricity price makes electrochemically driven CO_2 utilization technologies potentially profitable for commercial applications.[12]

Recent studies in electrocatalytic CO_2 reduction have been primarily focused on high-value multicarbon (C_{2+}) products, such as ethylene, ethanol, and *n*-propanol.[13–16] Among all the catalysts, copper (Cu) is the most widely studied CO_2 reduction catalyst with a relatively high C_{2+} selectivity.[17–21] Therefore, many efforts have been devoted to exploring nanostructured Cu catalysts such as nanoparticles,[14,22,23] nanofoam,[24,25] nanowires,[26,27] and nanopores[28] to further elucidate the structure-property correlation for CO_2 reduction over Cu catalysts. However, most of these investigations are typically performed in batch-cell configurations which have some technical limitations. For example, the low solubility of CO_2 in electrolyte (usually an aqueous solution) greatly limits the maximum CO_2 reduction current density to ≈40 mA cm^{-2}, making it difficult to examine catalytic behavior at more practical current densities (>200 mA cm^{-2}).[29,30] In addition, because batch-cell type studies often utilize CO_2 saturated electrolytes, it is not possible to use alkaline electrolytes because hydroxide ions strongly react with dissolved CO_2 to form carbonates. In order to overcome these challenges associated with batch-cell type configurations, a flow cell configuration can be utilized,[31] which has been recently demonstrated for silver catalyzed CO_2 reduction to CO.[32,33] Despite these efforts, there is currently no systematic flow cell study on how nanostructuring and electrolyte can affect CO_2 reduction properties of Cu catalysts, especially in alkaline electrolytes.

In this work, we synthesized a nanoporous Cu catalyst with a pore size of 100–200 nm and examined its catalytic properties for CO_2 reduction in a microfluidic electrolysis cell. At an applied

J.-J. Lv, M. Jouny, W. Luc, Dr. W. L. Zhu, Prof. F. Jiao
Center for Catalytic Science & Technology
Department of Chemical & Biomolecular Engineering
University of Delaware
Newark, DE 19716, USA
E-mail: jiao@udel.edu
J.-J. Lv, Prof. J.-J. Zhu
State Key Laboratory of Analytical Chemistry for Life Science
School of Chemistry and Chemical Engineering
Nanjing University
Nanjing 210093, P. R. China

**ADVANCED
SCIENCE NEWS**

www.advancedsciencenews.com

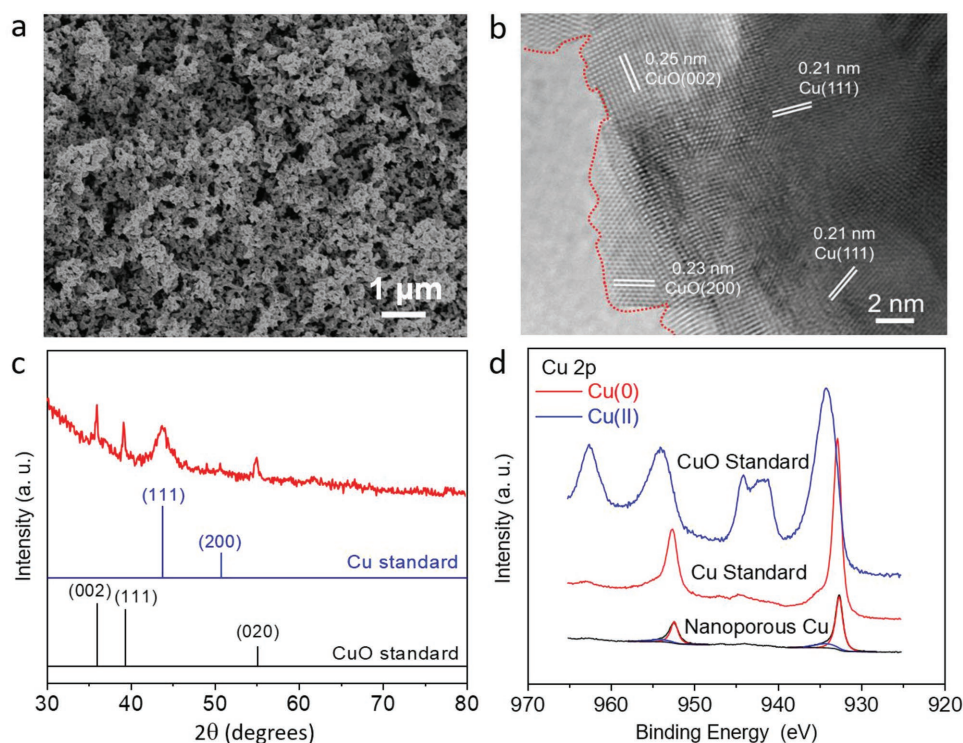**ADVANCED
MATERIALS**

www.advmat.de

Figure 1. Characterization of nanoporous Cu catalyst. a) A typical SEM image, b) a typical HRTEM image (red dash line indicates the rough particle surface), c) PXRD patterns (standards were also shown for comparison), and d) XPS spectra (CuO and Cu standards were added for comparison).

potential of −0.67 V versus reversible hydrogen electrode (RHE), the catalyst exhibited a total Faradaic efficiency (FE) of 79% for CO_2 reduction products at a current density of 653 mA cm^{-2}. An FE of 62% for C_{2+} products was achieved together with a C_{2+} partial current density exceeding 400 mA cm^{-2}, which is among the highest C_{2+} partial current densities that have ever been obtained in CO_2 electrolysis. Moreover, a variety of electrolytes (KOH, KHCO$_3$, KCl, and K$_2$SO$_4$) were also investigated, and the results demonstrated that CO_2 reduction in alkaline electrolyte (i.e., KOH) exhibited the highest C_{2+} FE. In the case of non-buffering electrolytes, the significant change in bulk pH due to the generation of hydroxide ions during high-rate electrolysis illustrates the uncertainty of the actual pH at the electrode–electrolyte interface during operating conditions and demonstrates the challenges associated with using the RHE scale. We also emphasize the need for further modeling of the complex triple-phase boundary at the electrode–electrolyte interface for a CO_2 flow cell electrolyzer.

Nanoporous Cu catalyst was synthesized by precipitating a Cu salt in an ammonia solution, followed by thermal annealing and in situ electrochemical reduction. In the first precipitation step, interconnected Cu(OH)$_2$ nanorods were synthesized (Figure S1a, Supporting Information) to form a fiber-like network (Figure S1b, Supporting Information). The high phase purity of Cu(OH)$_2$ was confirmed by powder X-ray diffraction (PXRD) analysis (Figure S1c, Supporting Information). The following thermal annealing step transformed the Cu(OH)$_2$ nanorods into porous CuO with 3D interconnected pores of 100–200 nm in diameter (Figure S2a–e, Supporting Information). The PXRD pattern confirmed the phase purity of monoclinic

CuO (Figure S2f, Supporting Information). N$_2$ adsorption–desorption measurement showed a Brunauer–Emmett–Teller surface area of 7.02 m^2 g^{-1} (Figure S3, Supporting Information). After deposition of the CuO sample onto a gas diffusion layer (GDL) and an in situ reduction treatment, a highly porous network was formed (**Figure 1**a), an essential property that is needed during high-rate CO_2 electrolysis due to the substantial generation of gaseous products at the gas diffusion electrode interface.

The atomic structure of the Cu catalyst was further examined using high resolution transmission electron microscopy (HRTEM) and PXRD techniques. The typical HRTEM images are shown in Figure 1b and Figure S4 in the Supporting Information where a polycrystalline nature of this catalyst was observed. The image clearly shows both metallic Cu and CuO domains, in which the particles were mostly metallic Cu whereas the surface was dominated by CuO. Additionally, the lattice fringes corresponding to Cu(111) were widely spread out through the sample, indicating the high population of the Cu(111) facet.[34,35] These observations were in good agreement with the PXRD analysis, where diffraction peaks for both metallic Cu and CuO phases were identified (Figure 1c). For the peaks corresponding to the Cu phase, the Cu(111) peak was much higher than the Cu(200) peak, suggesting the predominant Cu(111) facet in the sample.[36,37] The oxidation state of Cu on the catalyst surface was also analyzed using X-ray photoelectron spectroscopy (XPS) technique. The XPS results (Figure 1d) showed a surface consisting of mostly metallic Cu with the presence of Cu^{2+}. It is important to note that because nanosized Cu can be readily oxidized by O$_2$, it is possible that
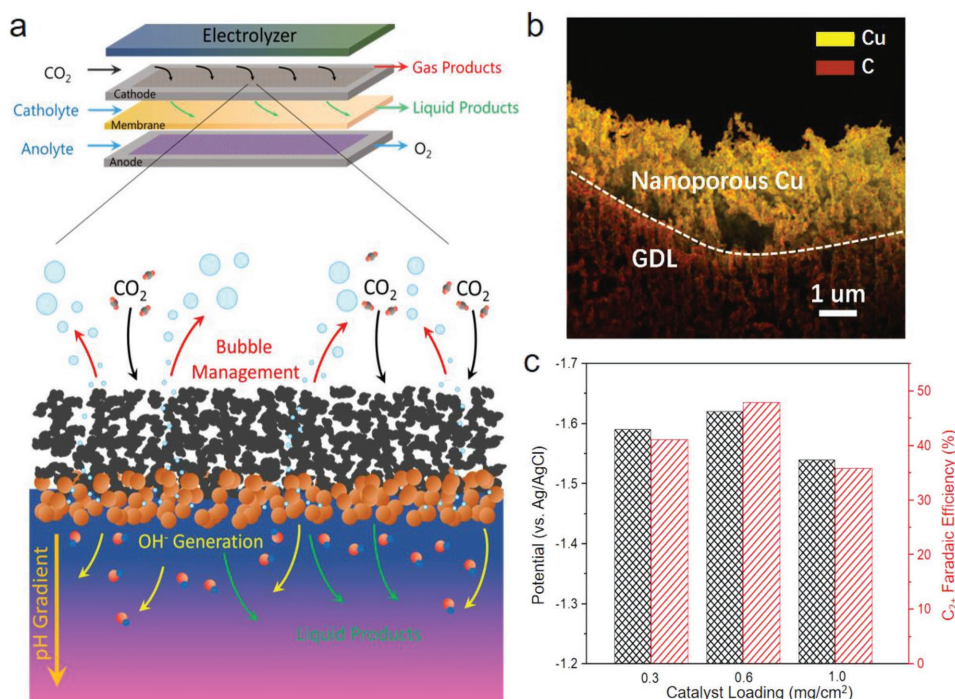
Figure 2. a) A diagram of the microfluidic electrolyzer with a zoomed-in schematic of the electrode–electrolyte interface illustrating how a highly porous structure facilitates bubble management, b) a cross-sectional SEM image of the nanoporous copper catalyst on GDL, and c) the influence of catalyst loading on the applied potential and FE at a constant current density of 200 mA cm^{-2}.

the observed CuO phase was formed during sample handling in air following in situ reduction. Future studies using surface sensitive operando techniques are required to determine the true surface nature of catalyst under reaction conditions.

The as-synthesized nanoporous Cu catalyst was investigated in a microfluidic flow cell electrolyzer, which was composed of two compartments for liquid electrolytes (catholyte and anolyte) and one gas compartment for CO_2 delivery and gas product collection (**Figure 2**a). This configuration allowed for CO_2 to be abundantly fed to the catalyst surface at the complex triple-phase boundary of the electrode–electrolyte interface which allowed for the investigation of CO_2 electrolysis at high current densities. However, one major challenge is managing the transport of gaseous products through the gas diffusion electrode during high rates of electrolysis to prevent bubble accumulation that would otherwise block catalytic sites. Therefore, maintaining a degree of porosity in the gas diffusion electrode is critical for allowing gaseous products to rapidly exit the reactor while achieving high current densities.[38] The porosity of the electrode is demonstrated by the cross-sectional field emission scanning electron microscopy (SEM) image shown in Figure 2b. As such, we investigated the loading effect of nanoporous copper by conducting CO_2 electrolysis under a constant current density (200 mA cm^{-2}) with different catalyst loadings and the results are summarized in Figure 2c. An optimum C_{2+} FE was observed with a catalyst loading of 0.6 mg cm^{-2}. Furthermore, for a catalyst loading of 1.0 mg cm^{-2}, the current profile was unstable due to insufficient porosity causing gaseous product bubbles to accumulate and block catalytic sites (Figure S5, Supporting Information). Therefore, we chose the 0.6 mg cm^{-2} catalyst loading for the rest of investigations. At

a catalyst loading of 0.6 mg cm^{-2}, stable current profiles are evident at a wide range of potentials (**Figure 3**a). The highest current density (656 mA cm^{-2}) was achieved at an applied potential of −0.66 V versus RHE (all the voltages are on the RHE scale unless stated otherwise).

Figure 3b shows the correlation between C_{2+} FE, C_{2+} partial current density, and applied potential, in which C_{2+} production through C−C coupling reaction is clearly favored at high overpotentials. At −0.67 V, we have successfully obtained a C_{2+} FE of 62% with a C_{2+} current density of 411 mA cm^{-2}. More importantly, a high CO_2 reduction FE of 79% was also achieved simultaneously with the high current density at −0.67 V. Product analysis showed that the majority of CO_2 reduction products were ethylene (38.6%), ethanol (16.6%), CO (14.7%), and n-propanol (4.5%) (Figure 3c). A small amount of acetate and formate were also produced. At less negative potential (vs RHE), the ethylene selectivity dropped significantly, whereas both CO and H_2 selectivities increased considerably. The trend suggests that C−C coupling is promoted at high overpotentials through the further conversion of surface bound CO, while suppressing hydrogen evolution during CO_2 electrolysis.

A comparison of the values in this work against literature values is shown in Figure S6 and Table S1 in the Supporting Information.[13,14,24,27,39–45] The nanoporous copper catalyst performance is among the best that has ever been achieved for CO_2 electroreduction to C_{2+} products. Attempts to operate the cell at higher overpotentials failed because the current profile became highly unstable, which was predominantly caused by electrolyte flooding and high-rate gas evolution at cathode. Additionally, the stability of CO_2 electrolysis using nanoporous Cu catalyst was investigated by conducting a continuous CO_2
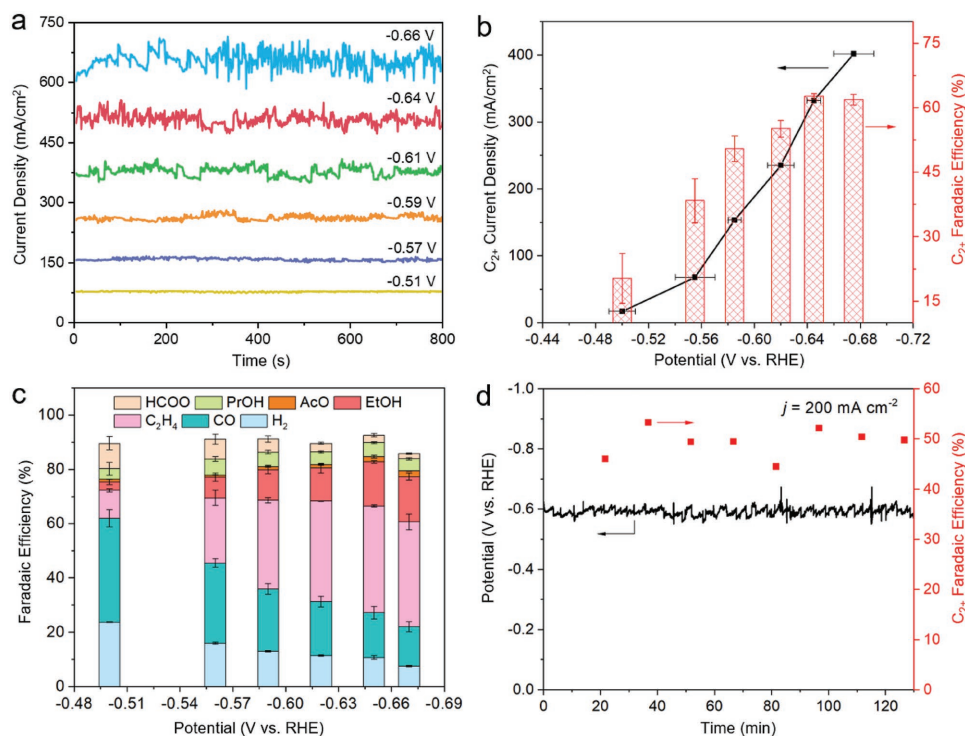
Figure 3. a) Chronoamperometric curves at various potentials for CO_2 reduction on nanoporous Cu in 1 M KOH electrolyte, b) C_{2+} partial current density for electrolysis of nanoporous Cu in 1 M KOH electrolyte, c) corresponding FEs, and d) the voltage profile and C_{2+} FEs at a constant current density of 200 mA cm^{-2}.

electrolysis under constant current mode at 200 mA cm^{-2}. The results (Figure 3d) showed a very stable potential profile over 2 h without any significant voltage change. The product distributions were almost identical over the course of 2 h electrolysis except the first 20 min, which could be due to initial activation (Figure S7, Supporting Information). Both the morphology and the composition of the nanoporous Cu electrode were maintained as indicated from postreaction SEM and XPS analysis (Figure S8, Supporting Information).

The influence of electrolyte and pH has been previously modeled and studied on Cu electrodes in batch-type electrochemical configurations.[46–49] However, these studies were conducted at relatively low current densities and are unable to utilize alkaline electrolytes that have been shown to enhance CO_2 reduction on Ag and Au catalysts.[32,50] Herein, we investigated the catalytic properties of nanoporous Cu in four different electrolytes, i.e., KOH, $KHCO_3$, KCl, and K_2SO_4. To isolate the anion effect, we held the K$^+$ concentration constant at 1 M for all the electrolytes. The bulk pH values were measured before and after electrolysis at each applied potential and are presented in Table S2 in the Supporting Information. For the KOH and $KHCO_3$ electrolytes, no significant pH changes were observed after electrolysis; whereas both KCl and K_2SO_4 electrolytes showed a substantial increase in pH, a change up to 4 pH units at high current densities. This is likely due to large quantity of hydroxide (OH$^-$) anions produced at cathode during high-rate CO_2 electrolysis which caused a significant increase in bulk pH for nonbuffering electrolytes (i.e., KCl and K_2SO_4). In contrast, a smaller increase in bulk pH was observed in 1 M $KHCO_3$ due to its buffering capabilities. In the case of KOH electrolyte, the amount of

OH$^-$ anions generated at cathode was negligible in comparison to the total quantity of OH$^-$ in the bulk electrolyte.

The CO_2 electrolysis results are presented in **Figure 4**a,b, where we calculated the applied potential at each current density using the pH value of the bulk electrolyte after electrolysis (Table S2, Supporting Information). Among all four electrolytes, the performance of KOH electrolyte was substantially better than those of other electrolytes in terms of C_{2+} current densities, overpotentials, and C_{2+} FE (Figure 4). A detailed product analysis for each electrolyte is provided in Table S3 in the Supporting Information. We attempted to operate the electrolyzer in KCl and K_2SO_4 electrolytes at higher overpotentials (i.e., higher current densities); however, the electrolyzer experienced high resistance, which quickly overloaded the system. The high resistance is likely due to the poor ionic conductivity of membrane in KCl and K_2SO_4 electrolytes. We also studied both anion exchange membrane and cation exchange membrane, with neither of them being conductive enough for high current densities. Future studies using a suitable membrane or a membrane-less cell are necessary to explore the CO_2 electrolysis performances using near-neutral pH electrolytes.

As evidenced by the significant increase in measured bulk pH, the OH$^-$ concentration at the catalyst surface is likely much higher than that of the bulk electrolyte under CO_2R conditions.[30,46,51,52] Therefore, a better method is needed to estimate the applied potentials on the RHE scale that accurately reflects the true pH at the electrode–electrolyte interface. At the alkaline triple-phase boundary in the flow cell, OH$^-$ hydrates CO_2 to form carbonates, leading to a complicated transport

**ADVANCED
SCIENCE NEWS**

www.advancedsciencenews.com
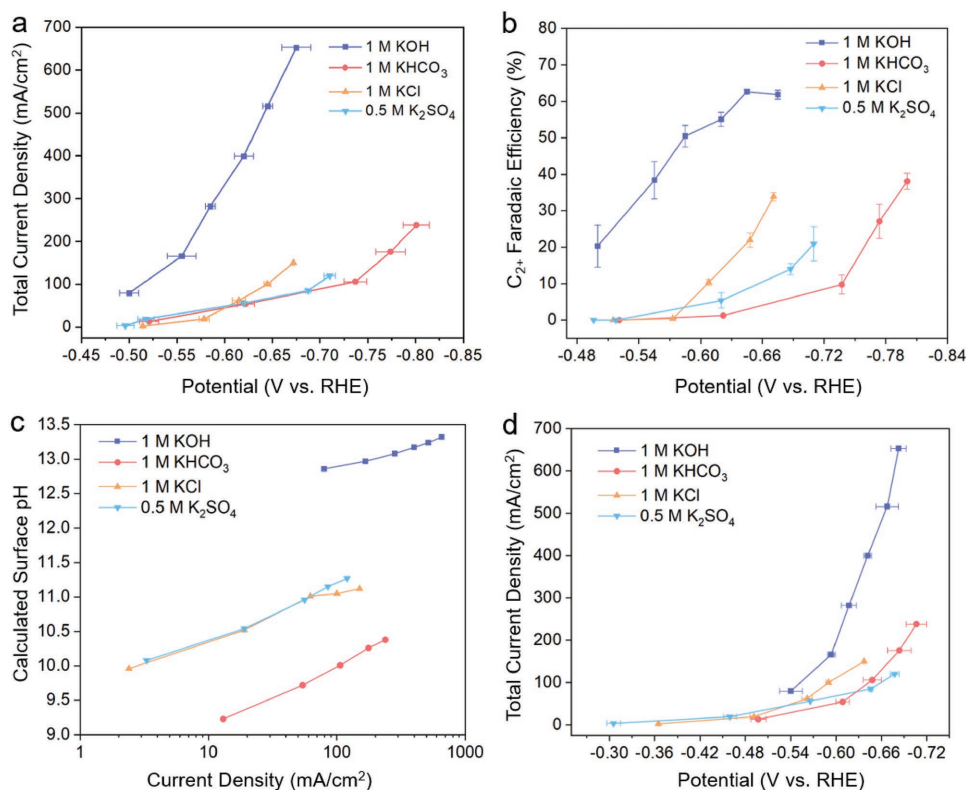
**ADVANCED
MATERIALS**

www.advmat.de

Figure 4. a) Total current density and b) C_{2+} FE for CO_2R of nanoporous Cu in different electrolytes. Note that the potentials (vs RHE) were estimated using the pH value of electrolyte exiting the flow cell. c) Calculated surface pH versus current density for different electrolytes and d) total reduction current density versus potential based on the calculated surface pH.

problem involving the diffusion of these reactive species between the CO_2/electrolyte interface near the catalyst surface and the bulk electrolyte. We estimated the surface pH for each electrolyte tested using a transport model similar to that recently demonstrated by Dinh et al. (see Supporting Information for calculation details).[45] The relationship between the applied current density and calculated surface pH for each electrolyte tested is shown in Figure 4c. For 1 M KOH, the surface pH is slightly reduced relative to the bulk pH due to significant carbonate formation near the catalyst surface. In contrast, the surface pH for the nonbuffering electrolytes (1 M KCl and 0.5 M K_2SO_4) is significantly higher than the bulk pH for all current densities. Furthermore, there is a strong correlation between the calculated surface pH and the production of C_{2+} products (Figure 4b), which is consistent with theoretical suggestions that near-surface OH^- facilitates C−C coupling for CO_2R.[45,49]

When the applied potential for CO_2R is referenced to RHE using the calculated surface pH (Figure 4d), the overpotential for KCl and K_2SO_4 became less than that of $KHCO_3$. The same set of results was also plotted using the potentials versus Ag/AgCl for comparison (Figure S10, Supporting Information). Interestingly, the trend in activity matches to some degree with the trend in electrolyte conductivity with $KOH>KCl>K_2SO_4>KHCO_3$ (Figure S11, Supporting Information). The conductivity may likely have a significant effect on the total current density by increasing the active triple-phase boundary area due to a lower resistance between thin electrolyte coating within the catalyst layer and the bulk electrolyte.[30]

As we mentioned previously, operating a microfluidic CO_2 electrolyzer at current densities higher than 650 mA cm^{-2} is challenging, which is due to the fact that CO_2 electrolysis at high rates (i.e., high current densities) produces tremendous amount of gaseous products that disturb and interrupt gas and ion diffusion pathways to/away from the catalytic sites. As a result, large quantity of liquid electrolyte is forced to the gas compartment causing significant flooding and internal resistance fluctuation. Although we have successfully achieved a stable operation at 200 mA cm^{-2} for more than 2 h, it is considerably difficult to maintain an efficient electrode–electrolyte interface at higher rates to ensure that both gaseous CO_2 and liquid electrolyte are in good contact with the solid catalyst.

Another technical challenge associated with the microfluidic CO_2 electrolysis cell is salt accumulation at the electrode–electrolyte interface, especially when a strong base (e.g., KOH) is used as catholyte. The performance degradation due to salt accumulation at the electrode–electrolyte interface has been previously reported in the case of Au catalyst.[50] In this work, a highly porous Cu catalyst was employed to improve the accessibility of catalyst surface (Figure 2a). However, the formation of carbonate salt still slowly blocked the pores of the catalyst and the GDL, causing substantial voltage losses and reactant/product transport issues at the interface.

Addressing these issues requires innovations in reactor engineering and catalyst design. For example, tuning the hydrophobicity of the GDL support and/or catalyst surface could potentially enhance the gas transport across the gas diffusion

electrode. Previous study has shown that the hydrophobicity of GDL strongly affected the cell performance in the case of CO_2 reduction to CO.[53] Using the same strategy, the efficiency of electrolyzer cell dedicated to C_{2+} products could be further improved. Moreover, understanding the pH and electrolyte effects at the electrode–electrolyte interface is also crucial to the design of new generation flow cell electrolyzers with a more robust interface. Strategies to minimize carbonate formation at interface by controlling the interfacial pH will benefit long-term operation of the microfluidic cell. Additionally, a more selective catalyst than Cu could suppress salt product formation (e.g., formate and acetate) if they are not desired products.

In summary, we have synthesized a nanoporous Cu catalyst, which exhibited high performance in a microfluidic CO_2 electrolyzer. At an applied potential of -0.67 V, we have achieved a current density of 653 mA cm^{-2} with a C_{2+} selectivity of 62%, which is among the best performances that have ever been achieved for CO_2 electroreduction to C_{2+} products. The systematic study of electrolyte effect showed that KOH exhibited much better performance than bicarbonate and other nonbuffer near-neutral electrolytes, suggesting that C−C coupling reaction on Cu are favored at high pH values. Further efforts are required to improve the interface robustness of the CO_2 electrolyzer in order to achieve long-term operation at industrially relevant rates.

Experimental Section

Synthesis of Nanoporous Copper: All chemicals were of analytical grade and used as received without further purification unless otherwise noted. The nanoporous copper were fabricated through the annealing of Cu(OH)$_2$ nanorods and the electrochemical reduction of the nanoporous CuO. Firstly, the Cu(OH)$_2$ nanorods were prepared by a literature method.[54] Typically, 1 g of Cu(NO$_3$)$_2$ is first dissolved in 100 mL distilled water. Then, 30 mL NH$_3$ H$_2$O (0.15 M) solution was added to the Cu(NO$_3$)$_2$ solution under constant stirring at room temperature. A blue precipitate of Cu(OH)$_2$ was produced when dropwise added 10 mL of NaOH (1 M) solution ($\approx$2 mL min^{-1}) to the above solution to adjust the pH value to 9–10. After 30 min, the blue Cu(OH)$_2$ precipitate was filtered washed several times to obtain a solid product, and then dried in the vacuum oven for overnight. Secondly, the nanoporous CuO was prepared by annealing the Cu(OH)$_2$ nanorods in the static air atmosphere at 500 °C for 2 h with a heating rate of 32 °C min^{-1}. At last, the nanoporous copper was obtained by the electrochemical reduction of nanoporous CuO on GDL at a constant current density of 10 mA cm^{-2} in the same cell as CO_2 reduction, and the corresponding applied voltages of different electrolyte were listed in the Table S7 in the Supporting Information.

Materials Characterization: The morphology and microstructure were characterized by SEM (Auriga, 1.5 kV), transmission electron microscopy (TEM), and HRTEM using a JEM-3010 TEM operating at 200 kV. The SEM images were taken directly by coating the sample on GDL (Fuel Cell Store). The TEM sample was acquired by scraping off from the nanoporous copper coated GDL. PXRD measurements were conducted on a D8 ADVANCE X-ray diffractometer (Bruker Corporation, America). To analyze the composition near the surface of the nanoporous Cu catalyst, the commercial CuO powder (98%, Sigma-Aldrich) and Cu foil (99.999%, Alfa-Aesar) were measured as control materials. A Thermo Scientific K-Alpha XPS System was used and XPS fitting was conducted by CasaXPS software with the adventitious carbon peak being calibrated to 284.8 eV. All peaks were fitted using a Gaussian/Lorentzian product line shape and a Shirley background.

Flow Cell Electrolysis: Electrochemical measurements were conducted on an Autolab potentiostat (PG128N) in a three-electrode system. In this study, the carbon paper with a microporous layer (Sigracet 29 BC, Fuel Cell Store) was used as the gas diffusion layer for supporting catalyst, collecting current and acting as a pathway for gas from flow channels to the catalyst surface. The IrO$_2$ coated GDL (loading: 0.5 mg cm^{-2}) was used as the counter electrode and Ag/AgCl (saturated KCl) as the reference electrode. The nanoporous-Cu-coated GDL was applied as the working electrode, which was prepared by hand-painting the nanoporous Cu catalyst ink as in previously reported work.[55,56] The GDL was weighed before and after deposition to record its actual catalyst loading. To prepare the catalyst ink, 25 mg of catalyst was ultrasonically dispersed in the mixture of 3 mL of *n*-propanol, 500 µL of carbon nanotube (CNT) solution (5 mg multiwalled CNT (MWCNT) (>98%, Sigma-Aldrich) dispersed in 5 mL tetrahydrofuran (THF)) and 20 µL of (10 wt% aqueous solution, Fuel Cell Store). The MWCNTs were used to facilitate oxide reduction and did not contribute to the electrocatalysis (Figure S12, Supporting Information). Then, the mixture was sonicated for 30 min.

CO_2 electrolysis was performed in a three-channel flow cell with channels of dimension $2 \times 0.5 \times 0.15$ cm^3. The electrode area was 1 cm^2 and the electrode to membrane distance was 1.5 mm. An external Ag/AgCl reference electrode (Pine Research) located $\approx$5 cm from the cathode was used to measure the cathodic half-cell potential. All potential measurements were converted to the RHE based on the following formula $E_{RHE} = E_{Ag/AgCl} + E^{\theta}_{Ag/AgCl} + 0.059 \times pH$ (in volts). The pH values of bulk electrolyte after electrolysis were used for RHE conversions unless stated otherwise. The device was fabricated from acrylic and included the gas channel for flowing CO_2, the anode and cathode channels for flowing electrolyte, the membrane for separating the anode and cathode, and solid end pieces (Figure S13, Supporting Information). Poly(tetrafluoroethylene) (PTFE) gaskets were placed between each component for sealing and the device was tightened using six bolts. The gas flow rate into the flow cell was set as 10 sccm via a mass flow controller (Brooks GF40). The catholyte flow rates were controlled via a peristaltic pump (Cole-Parmer), with the catholyte flow rate ranging from 0.1 to 1 mL min^{-1} depending on the current density (lower flow rates were used at lower current densities to allow for sufficient accumulation of liquid products). The anolyte flow rate was 2 mL min^{-1}. An anion exchange membrane (FAA-3, Fumatech) was used in KOH and KHCO$_3$ electrolyte, and a proton exchange membrane (Nafion, Fumatech) was used in KCl and K$_2$SO$_4$ electrolyte. The backpressure of the gas in the flow cell was tuned to atmospheric pressure by adding vacuum as controlled by a backpressure controller (Cole-Parmer). Each reported data point reflected the mean of at least three measurements, where the error bars were the standard deviation.

Gas products were quantified on a Multigas #5 GC (SRI Instruments) equipped with a HayeSep D and Molsieve 5A columns connected to a thermal conductivity detector (TCD) and a HayeSep D column connected to a flame ionization detector (FID). Hydrogen was quantified using TCD, while ethylene, carbon monoxide (for CO_2 electrolysis), and methane were detected on both FID and TCD. The low concentration of ethylene and CO was detected by FID after using a methanizer. The FE for products was calculated using the following equation:

$$FE(\%) = \frac{nFxV}{j_{Tot}} \times 100 \tag{1}$$

where n = # of electrons transferred

F = Faraday's constant
x = mole fraction of product
V = total molar flow rate of gas
j_{Tot} = total current

Liquid products were quantified using a Bruker AVIII 600 MHz NMR spectrometer. Typically, 500 µL of collected diluted catholyte was mixed with 100 µL of internal standard solution (20 ppm (m/m) dimethyl sulfoxide (≥99.9%, Alfa Aesar) in D$_2$O). The 1D ^{1}H spectrum was measured with water suppression using a presaturation method.

Supporting Information

Acknowledgements

Conflict of Interest

The authors declare no conflict of interest.

Keywords

[1] N. S. Lewis, D. G. Nocera, *Proc. Natl. Acad. Sci.*, USA **2006**, *103*, 15729.

[2] M. Y. He, Y. H. Sun, B. X. Han, *Angew. Chem., Int. Ed.* **2013**, *52*, 9620.

[3] M. D. Porosoff, B. H. Yan, J. G. G. Chen, *Energy Environ. Sci.* **2016**, *9*, 62.

[4] H. Arakawa, M. Aresta, J. N. Armor, M. A. Barteau, E. J. Beckman, A. T. Bell, J. E. Bercaw, C. Creutz, E. Dinjus, D. A. Dixon, K. Domen, D. L. DuBois, J. Eckert, E. Fujita, D. H. Gibson, W. A. Goddard, D. W. Goodman, J. Keller, G. J. Kubas, H. H. Kung, J. E. Lyons, L. E. Manzer, T. J. Marks, K. Morokuma, K. M. Nicholas, R. Periana, L. Que, J. Rostrup-Nielson, W. M. H. Sachtler, L. D. Schmidt, A. Sen, G. A. Somorjai, P. C. Stair, B. R. Stults, W. Tumas, *Chem. Rev.* **2001**, *101*, 953.

[5] E. V. Kondratenko, G. Mul, J. Baltrusaitis, G. O. Larrazabal, J. Perez-Ramirez, *Energy Environ. Sci.* **2013**, *6*, 3112.

[6] W. H. Wang, Y. Himeda, J. T. Muckerman, G. F. Manbeck, E. Fujita, *Chem. Rev.* **2015**, *115*, 12936.

[7] Q. Lu, F. Jiao, *Nano Energy* **2016**, *29*, 439.

[8] J. Qiao, Y. Liu, F. Hong, J. Zhang, *Chem. Soc. Rev.* **2014**, *43*, 631.

[9] C. Costentin, M. Robert, J. M. Saveant, *Acc. Chem. Res.* **2015**, *48*, 2996.

[10] N. M. Haegel, R. Margolis, T. Buonassisi, D. Feldman, A. Froitzheim, R. Garabedian, M. Green, S. Glunz, H. M. Henning, B. Holder, I. Kaizuka, B. Kroposki, K. Matsubara, S. Niki, K. Sakurai, R. A. Schindler, W. Tumas, E. R. Weber, G. Wilson, M. Woodhouse, S. Kurtz, *Science* **2017**, *356*, 141.

[11] H. W. Ryan, B. Mark, *2016 Wind Technologies Market Report*, Report number LBNL-2001042, U.S. Department of Energy, August **2017**.

[12] M. Jouny, W. Luc, F. Jiao, *Ind. Eng. Chem. Res.* **2018**, *57*, 2165.

[13] T. T. H. Hoang, S. Verma, S. Ma, T. T. Fister, J. Timoshenko, A. I. Frenkel, P. J. A. Kenis, A. A. Gewirth, *J. Am. Chem. Soc.* **2018**, *140*, 5791.

[14] S. Ma, M. Sadakiyo, R. Luo, M. Heima, M. Yamauchi, P. J. A. Kenis, *J. Power Sources* **2016**, *301*, 219.

[15] R. G. Mariano, K. McKelvey, H. S. White, M. W. Kanan, *Science* **2017**, *358*, 1187.

[16] A. J. Garza, A. T. Bell, M. Head-Gordon, *ACS Catal.* **2018**, *8*, 1490.

[17] X. Liu, J. Xiao, H. Peng, X. Hong, K. Chan, J. K. Nørskov, *Nat. Commun.* **2017**, *8*, 15438.

[18] Y. Lum, Y. Kwon, P. Lobaccaro, L. Chen, E. L. Clark, A. T. Bell, J. W. Ager, *ACS Catal.* **2016**, *6*, 202.

[19] R. B. Sandberg, J. H. Montoya, K. Chan, J. K. Nørskov, *Surf. Sci.* **2016**, *654*, 56.

[20] K. J. P. Schouten, Y. Kwon, C. J. M. van der Ham, Z. Qin, M. T. M. Koper, *Chem. Sci.* **2011**, *2*, 1902.

[21] X. Huang, Y. Li, Y. Li, H. Zhou, X. Duan, Y. Huang, *Nano Lett.* **2012**, *12*, 4265.

[22] A. Loiudice, P. Lobaccaro, E. A. Kamali, T. Thao, B. H. Huang, J. W. Ager, R. Buonsanti, *Angew. Chem., Int. Ed.* **2016**, *55*, 5789.

[23] O. A. Baturina, Q. Lu, M. A. Padilla, L. Xin, W. Li, A. Serov, K. Artyushkova, P. Atanassov, F. Xu, A. Epshteyn, T. Brintlinger, M. Schuette, G. E. Collins, *ACS Catal.* **2014**, *4*, 3682.

[24] A. Dutta, M. Rahaman, N. C. Luedi, M. Mohos, P. Broekmann, *ACS Catal.* **2016**, *6*, 3804.

[25] S. Sen, D. Liu, G. T. R. Palmore, *ACS Catal.* **2014**, *4*, 3091.

[26] Y. Li, F. Cui, M. B. Ross, D. Kim, Y. Sun, P. Yang, *Nano Lett.* **2017**, *17*, 1312.

[27] M. Ma, K. Djanashvili, A. Smith Wilson, *Angew. Chem., Int. Ed.* **2016**, *55*, 6680.

[28] Y. Peng, T. Wu, L. Sun, J. M. V. Nsanzimana, A. C. Fisher, X. Wang, *ACS Appl. Mater. Interfaces* **2017**, *9*, 32782.

[29] Y. Chen, N. S. Lewis, C. Xiang, *Energy Environ. Sci.* **2015**, *8*, 3663.

[30] M. R. Singh, E. L. Clark, A. T. Bell, *Phys. Chem. Chem. Phys.* **2015**, *17*, 18924.

[31] D. M. Weekes, D. A. Salvatore, A. Reyes, A. X. Huang, C. P. Berlinguette, *Acc. Chem. Res.* **2018**, *51*, 910.

[32] S. Verma, X. Lu, S. Ma, R. I. Masel, P. J. A. Kenis, *Phys. Chem. Chem. Phys.* **2016**, *18*, 7075.

[33] S. Ma, R. Luo, J. I. Gold, A. Z. Yu, B. Kim, P. J. A. Kenis, *J. Mater. Chem. A* **2016**, *4*, 8573.

[34] Q. Xiao, L. Watson Brian, H. Dauskardt Reinhold, *Adv. Mater. Interfaces* **2016**, *3*, 1600118.

[35] Y. Chang, M. L. Lye, H. C. Zeng, *Langmuir* **2005**, *21*, 3746.

[36] A. Primo, I. Esteve-Adell, J. F. Blandez, A. Dhakshinamoorthy, M. Álvaro, N. Candu, S. M. Coman, V. I. Parvulescu, H. García, *Nat. Commun.* **2015**, *6*, 8561.

[37] L. De Trizio, A. Figuerola, L. Manna, A. Genovese, C. George, R. Brescia, Z. Saghi, R. Simonutti, M. Van Huis, A. Falqui, *ACS Nano* **2012**, *6*, 32.

[38] J. Herranz, J. Durst, E. Fabbri, A. Patru, X. Cheng, A. A. Permyakova, T. J. Schmidt, *Nano Energy* **2016**, *29*, 4.

[39] T. T. H. Hoang, S. Ma, J. I. Gold, P. J. A. Kenis, A. A. Gewirth, *ACS Catal.* **2017**, *7*, 3313.

[40] P. De Luna, R. Quintero-Bermudez, C.-T. Dinh, M. B. Ross, O. S. Bushuyev, P. Todorović, T. Regier, S. O. Kelley, P. Yang, E. H. Sargent, *Nat. Catal.* **2018**, *1*, 103.

[41] C. Hahn, T. Hatsukade, Y.-G. Kim, A. Vailionis, J. H. Baricuatro, D. C. Higgins, S. A. Nitopi, M. P. Soriaga, T. F. Jaramillo, *Proc. Natl. Acad. Sci.*, USA **2017**, *114*, 5918.

[42] H. S. Jeon, S. Kunze, F. Scholten, B. Roldan Cuenya, *ACS Catal.* **2018**, *8*, 531.

[43] K. Jiang, R. B. Sandberg, A. J. Akey, X. Liu, D. C. Bell, J. K. Nørskov, K. Chan, H. Wang, *Nat. Catal.* **2018**, *1*, 111.

[44] D. Ren, B. S.-H. Ang, B. S. Yeo, *ACS Catal.* **2016**, *6*, 8239.

[45] C.-T. Dinh, T. Burdyny, M. G. Kibria, A. Seifitokaldani, C. M. Gabardo, F. P. García de Arquer, A. Kiani, J. P. Edwards, P. De Luna, O. S. Bushuyev, C. Zou, R. Quintero-Bermudez, Y. Pang, D. Sinton, E. H. Sargent, *Science* **2018**, *360*, 783.

**ADVANCED
SCIENCE NEWS**

www.advancedsciencenews.com

**ADVANCED
MATERIALS**

www.advmat.de

[46] J. Resasco, Y. Lum, E. Clark, Z. Zeledon Jose, T. Bell Alexis, *ChemElectroChem* **2018**, *5*, 1064.

[47] R. Kas, R. Kortlever, H. Yılmaz, M. T. M. Koper, G. Mul, *ChemElectroChem* **2015**, *2*, 354.

[48] J. Resasco, L. D. Chen, E. Clark, C. Tsai, C. Hahn, T. F. Jaramillo, K. Chan, A. T. Bell, *J. Am. Chem. Soc.* **2017**, *139*, 11277.

[49] K. J. P. Schouten, E. P. Gallent, M. T. M. Koper, *J. Electroanal. Chem.* **2014**, *716*, 53.

[50] S. Verma, Y. Hamasaki, C. Kim, W. Huang, S. Lu, H.-R. M. Jhong, A. A. Gewirth, T. Fujigaya, N. Nakashima, P. J. A. Kenis, *ACS Energy Lett.* **2018**, *3*, 193.

[51] A. S. Varela, M. Kroschel, T. Reier, P. Strasser, *Catal. Today* **2016**, *260*, 8.

[52] N. Gupta, M. Gattrell, B. MacDougall, *J. Appl. Electrochem.* **2006**, *36*, 161.

[53] B. Kim, F. Hillman, M. Ariyoshi, S. Fujikawa, P. J. A. Kenis, *J. Power Sources* **2016**, *312*, 192.

[54] G. H. Du, G. Van Tendeloo, *Chem. Phys. Lett.* **2004**, *393*, 64.

[55] B. Kim, S. Ma, H.-R. Molly Jhong, P. J. A. Kenis, *Electrochim. Acta* **2015**, *166*, 271.

[56] M. Jhong Huei-Ru, R. Brushett Fikile, J. A. Kenis Paul, *Adv. Energy Mater.* **2013**, *3*, 589.